Vacuum 202 (2022) 111162

Contents lists available at ScienceDirect

Vacuum

journal homepage: www.elsevier.com/locate/vacuum

Theoretical calculation and experimental verification of the vacuum thermal decomposition process of lunar silicon oxide

Chen Li [a,b], Kuixain Wei [a,*], Yang Li [b,d,**], Wenhui Ma [a,c], Sizhe Zhao [b], Han Yu [a], Zhuang Guo [b], Jianzhong Liu [b,d]

[a] Faculty of Metallurgical and Energy Engineering, Kunming University of Science and Technology, Kunming, 650093, China
[b] Center for Lunar and Planetary Sciences, Institute of Geochemistry, Chinese Academy of Sciences, Guiyang, 550081, China
[c] National Engineering Laboratory for Vacuum Metallurgy, Kunming University of Science and Technology, Kunming, 650093, China
[d] Center for Excellence in Comparative Planetology, Chinese Academy of Sciences, Hefei, 230026, China

ARTICLE INFO

Keywords:
Thermodynamic calculation
Vacuum thermal decomposition
Laser heating
Silicon oxide

ABSTRACT

Thermal decomposition of oxides can be achieved at a lower temperature under vacuum condition. For In Situ Resource Utilization (ISRU), using the thermal decomposition method to obtain resources can avoid complex processing. This study, through thermodynamic equilibrium calculation found that oxides such as iron(II) oxide (FeO), and magnesium oxide (MgO), are easy to decompose. While oxides, such as silicon monoxide (SiO), titanium(II) oxide (TiO), *etc*., are difficult to decompose. Silicon dioxide (SiO_2) is selected as the sample for the nanosecond laser experiment under a vacuum. Temperature simulation showed that a laser can give the sample high-temperature energy above 4700 K. Dynamic analysis showed that the sample undergoing complete plasma decomposition was the most thorough. The results of thermal decomposition of silicon monoxide is the most difficult to achieve. Under the conditions of 75 mJ laser pulse energy, 10^{-4} Pa initial vacuum, *etc*., the oxygen-silicon atom ratio of the products ranged from 1.74 to 0.12 and decreased with decreasing particle radius. Understanding the decomposition behavior of lunar surface oxides is crucial for the clean utilization of lunar surface resources. Moreover, it also provides a theoretical basis for high-temperature processing and element migration of airless objects.

1. Introduction

The Moon is the Earth's only natural satellite, orbiting our planet at an average distance of 384,400 km. It was the first target for human exploration of the solar system. The construction of a base of operation for long-term presence and research on the Moon requires metals, oxygen, and other resources to set up and maintain. Long-distance transportation from the Earth increases costs and risks. The lunar crust, like that of the Earth, is composed of a variety of oxides, and its types of resources and reserves can meet the needs of engineering. In Situ Resource Utilization (ISRU) in space is the most important method to establish a lunar base and achieve an interstellar settlement. Due to the limited availability of actual lunar soil and rock samples, there is currently no large-scale natural ore deposit that can be directly exploited and utilized [1]. On the one hand, the lunar surface has the environmental conditions of low gravity and high vacuum. On the other hand, the electrical properties and complex chemical composition of lunar soil pose great difficulties in mineral separation and purification [2]. Such difficulties render the original metallurgical processes unsuitable for extracting metals from the ore in space, which makes it extremely difficult for ISRU of metal resources in space.

Therefore, a series of metal extraction processes suitable for ISRU is needed. Feasible metal extraction processes include reduction, electrolysis, thermal decomposition, *etc*. In the process of carbothermal reduction, reducing agents may be deposited on lunar soil particles or lost due to the formation of carbides during the process [3] Although lunar soil contains C injected by the solar wind, its mass fraction is only 200×10^{-6} [1], which is not enough to meet the needs of the smelting process [4–6]. Hydrogen reduction is mainly used to extract Fe from ilmenite, mainly due to the inability of H_2 to reduce TiO_2 to prepare Ti thermodynamically. In addition, there are no experimental results on the production of hydrogen on the Moon [7,8]. Electrolysis can

* Corresponding author. Faculty of Metallurgical and Energy Engineering, Kunming University of Science and Technology, Kunming, 650093, China.
** Corresponding author. Center for Lunar and Planetary Sciences, Institute of Geochemistry, Chinese Academy of Sciences, Guiyang, 550081, China.
E-mail addresses: kxwei2008@hotmail.com (K. Wei), liyang@mail.gyig.ac.cn (Y. Li).

https://doi.org/10.1016/j.vacuum.2022.111162
Received 7 March 2022; Received in revised form 6 May 2022; Accepted 7 May 2022
Available online 13 May 2022
0042-207X/

overcome the thermodynamic limitations of the reduction method [9]. Most of the metals present in lunar soil can be extracted by the molten salt electrochemical method, which involves using a suitable molten salt system. However, the continuous operation of a molten salt electrolysis system requires the corresponding molten salt media, which are volatile halides and are frequently affected by impurities. Another electrolysis process suitable for ISRU is molten oxide electrolysis (MOE), which takes place at a melting temperature over the melting point of the oxides. This process does not require any form of supporting electrolyte. Instead, it has high requirements for inert electrode materials [10–13].

Different from the above methods, the thermal decomposition only requires electric heating and does not require auxiliary materials, thus it is generally considered to be a more feasible method for ISRU in space. This extraction method is almost impossible to perform on earth, but the ultra-high vacuum environment of the lunar surface facilitates the decomposition process. Since the vacuum environment can greatly promote the thermodynamic production of gases, this decomposition often occurs in the surface layer of lunar soil. One of the main reasons for the formation of primary nano metallic iron on the surface of Moon through weathering is the formation of vapor deposition after decomposition by different forms of energy input [14–16]. Sasaki et al. performed a thermal decomposition reaction, and designed a laser equipment to decompose olivine to obtain elemental iron [17]. Experiments by many research groups fully confirmed the feasibility of thermal decomposition and its significance in the process of space weathering [18–23]. The thermal decomposition method has received considerable attention by researchers due to its short process time and requirement for less equipment, including using a solar light source as a heat source that can be focused directly. Due to the existence of intermediate oxides, the process of extracting a metal by thermal decomposition is greatly restricted. Therefore, at lower temperature only intermediate oxides, except for a small amount of Fe in solid product, are obtained [24–26]. In order to perform a more complete decomposition reaction, Yabe et al. used different heat source to decompose magnesium oxide (MgO) in vacuum or in a protective atmosphere [27–29]. The decomposition of MgO can be verified by the hydrogen producing reaction between the product and water [30–32]. Then, Tanaka et al. measured the experimental temperature and energy efficiency of laser decomposition of Al_2O_3 in vacuum [33,34]. Although the characterization of the product was not perfect, this approach provides a feasible, cost-effective option for the application of the thermal decomposition method for ISRU in space. As a result, *in situ* extraction of resources by vacuum thermal decomposition does not involve a complicated process flow, and has the minimum space load, operation and maintenance cost.

In order to study the thermal decomposition behavior more thoroughly, this study uses the following methods to overcome the difficulties encountered in previous studies. Using thermodynamic analysis to better understand the properties, and decomposition behavior and conditions of different oxides. The products were collected and analyzed *in situ* by microanalysis to obtain the quantitative results and derive the qualitative rules. This work can better guide the research on ISRU.

2. Material and methods

The samples of SiO_2 were selected from a natural quartz mine. They are used as a simulant of SiO_2 in lunar soil.

The X-ray diffraction analysis pattern of the raw material shown in Fig. 1 reveals that the overall crystallinity of quartz ore is well organized, the main peak is high, and the peak type is sharp. The pattern indicates that the quartz ore crystal grows well along the crystal plane under relatively stable conditions, which is in line with the characteristics of natural silica ore. A comparison of the diffraction peaks reveal that there are two crystal forms, namely α quartz and β quartz, which same to lunar minerals [1]. The quartz with both crystal types belongs to low-temperature quartz, and the ore-forming temperature is lower. No other crystal forms of silica, such as tridymite and cristobalite, were found.

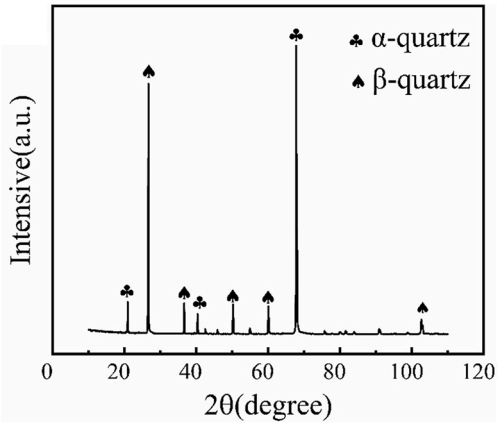

Fig. 1. X-ray diffraction pattern of silicon dioxide.

Low-temperature quartz, regardless of whether it is α quartz and β quartz of different point groups, has a similar crystal structure, only the difference in the crystal plane angle, and its chemical properties are close to that of high-temperature quartz. Therefore, it can be considered that the chemical properties of the silica raw material are uniform. The raw material silica can be explained based on its chemical composition analysis and X-ray diffraction (XRD) analysis, and represents the low-temperature quartz in terms of chemical purity and chemical properties.

The main impurity component of quartz is SiO_2, as determined by inductively coupled plasma atomic emission spectroscopy (ICP-AES). The impurity elements present at more than 1 ppmw are Fe, Al, and K, and the highest level is Fe (280 ppmw). SiO_2 accounts for more than 99.9% of the total content (Table 1).

In order to quantify the H content in quartz, the hydroxyl and water molecules in quartz minerals were tested using a quantitative method of Fourier Transform Infrared (FTIR) Spectroscopy. The hydroxyl and water peaks are in the interval 2800-3750 cm^{-1} and are often present as bun peaks. The hydroxyl group, which is homogeneous, is generally present at the lower wavenumber peaks, while the molecular water is present at the higher wavenumber peaks.

Quantitative testing of infrared spectra follows the Lambert-Bier law, i.e.

$$A_h = \varepsilon_h c t$$

Where A_h is the peak height after subtracting the baseline from the highest value within the broad peak of the absorbance, c is the content of the corresponding absorbing group, ε_h is the absorption coefficient of the peak height measurement method and t is the thickness of the sample.

Thus, the content of the absorbing group in the infrared spectrum can be expressed as

$$c = A_h / \varepsilon_h t$$

For quartz minerals, the Lambert-Bier equation corresponding to the water and hydroxyl content is [35]:

H_2O content in quartz (ppmw) = 840 × absorbance at 3400 cm^{-1}/ d (mm).

Natural quartz blocks were made into 1 cm^2 sheets, ground and polished to a final average thickness of approximately 358 μm, ultrasonically cleaned with anhydrous ethanol and then dried in a blast oven

Table 1
Composition analysis of sample of raw material.

Composition	SiO_2	Fe	Al	K
wt.%	>99.9	0.028	0.01	0.014

at 120 °C for 12 h to remove any water or hydroxyl groups introduced in the preparation of the samples. The samples were tested using an FEI-Nicolet Continuum model infrared spectrometer modified with a protective atmosphere. The samples were dried again with a heat lamp and immediately placed in the IR test chamber, after which the sample surface was cleaned with dry air (filtered by the dryer) for 40 min and tested for IR transmission spectroscopy after the atmospheric background was almost free of water peaks. A maximum wavenumber of 8000 cm^{-1} and a minimum wave number of 1400 cm^{-1} were chosen and the number of scans was set at a resolution of 4 for 256 (data interval of 0.482 cm^{-1}) and three random positions were selected for testing to ensure representative results. The preliminary test results are shown in Fig. 2, where it can be found that the hydroxyl group has a weak peak in the IR transmission spectrum. The absolute peak height of the absorbance can be obtained by zooming in on the 2600 - 4200 cm^{-1} wavenumber range and adding some of the baseline (Fig. 2). Combined with the Lambert-Bier absorption law, an accurate value for the water content of the quartz mineral is measured.

The absorptivity peak heights for the three measurements were 0.076, 0.030, and 0.045 respectively, indicating that the H content was not perfectly uniform in the sample, consistent with the characteristics of natural quartz. Substituting the results into the equations gives the following H and H_2O contents in the samples. Thus, the water content of the raw quartz ore is approximately 70.4–178.3 ppmw similar to the water content in lunar surface minerals (47–600 ppmw) [36] and the H content is approximately 7.8–19.8 ppmw. Although the lunar surface is part of a nominally water-free environment, the constant solar wind irradiation (the solar wind is primarily a plasma of H and He) has modified the H content of minerals during their long exposure history. This phenomenon continues on the surfaces of atmosphere-free objects and is known in astronomical and planetary science as solar wind injection [37].

The sample was cut with a diamond wire cutting machine and processed into a 1 cm^3 cube. The sample was cleaned with absolute ethanol and ultrasonication for 20 min. Then, the surface was polished, cleaned with absolute ethanol, followed by deionized water, and dried at 120 °C for 24 h to remove the impurities introduced during the processing process and release some gas impurities (H、O etc) adsorbed on the surface. The vacuum laser equipment used is shown in Fig. 3. The laser controller can control the Nd-YAG laser power to send out laser and adjust it in a certain range. The laser is generated from the Nd-YAG and emitted through the aperture. For a stable pulsed laser beam, the output power can be measured quantitatively 10 times by an external energy monitor. Then, the average value and fluctuation range of the laser output energy are obtained. The output beam is converged and refracted to the sample in the vacuum cavity through the focalizer. It is observed that during the measurement of the energy of the laser beam through the lens and then irradiation on the sample, some of the energy will be lost.

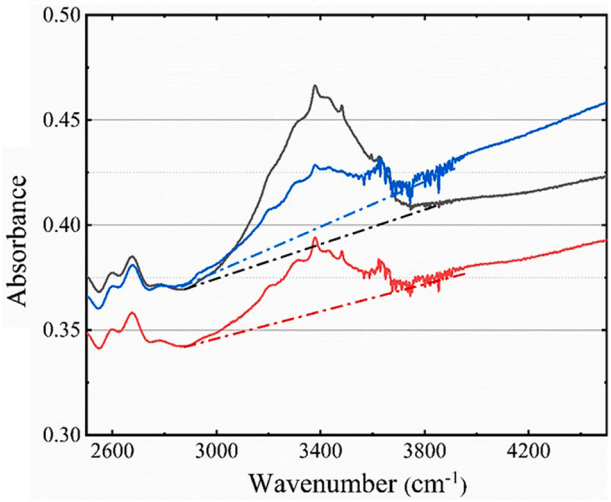

Fig. 2. FTIR transmission spectroscopy of quartz flakes (three tests).

For the vacuum environment of the experiments, after placing the sample inside the chamber, we used six symmetrically distributed flange valves to close the hatch with copper seals. Afterward, nitrogen gas is introduced for a period of up to 30 min to completely remove the effects of the little amount of water vapor that enters with the hatch open for a short period of time, while the laboratory is air-conditioned to ensure a constant temperature and humidity. At the end of the gas exchange, a mechanical pump is used to pre-evacuate the chamber and a molecular pump is used to create a higher vacuum for 4–5 h to achieve a maximum of 10^{-5}-10^{-6} Pa. The pulsed laser is adjusted at the beginning of the experiment to focus and form a certain angle of inclination with the sample, and after several tests, the experimental conditions are adjusted. At the start of the pulsed laser irradiation, the air pressure in the cavity rises instantaneously to 10^{-2}-10^{-3} Pa and then returns to 10^{-4} Pa within 1 s. This indicates that gas is being generated, the laser irradiation is at the ns level of time, but the change in air pressure has a significant hysteresis. Therefore, a frequency of 0.2 Hz implies a 5 s interval that allows a stable recovery to 10^{-4} Pa in the vacuum bin, hence the experimental conditions at a pressure of 10^{-4} Pa.

A 532-nm wavelength laser with an energy of 75 mJ (±5 mJ) and a frequency of 0.2 Hz was used to decompose the sample. In a pulse period, the decomposed solid materials are collected *in situ* through the copper mesh, and the decomposed gas cannot be collected due to the molecular pump. The gas can be determined by thermodynamic calculation and the reading of the vacuum system.

The crystal structure of the raw material was analyzed by XRD analysis, and ICP-AES to determine the type and content of impurities, respectively. The irradiated samples were observed using the dual-beam system. The dual-beam system combines SEM, focused ion beam (FIB), and energy dispersive X-ray spectroscopy (EDS). The morphology and chemical composition of the laser-irradiated area were analyzed by SEM-EDS. The raw material was excavated using a 30 kV voltage focused ion beam, polished with a 2 kV voltage focused ion beam. Then, ultra-thin slices were prepared for transmission electron microscopy (TEM) imaging. The final thickness was less than 100 nm, which was used as the standard sample to correct the energy spectrum data. TEM was used to obtain the image and EDS of the product.

3. Results and discussion

3.1. Lunar soil vacuum thermodynamic calculation

The process of vacuum thermal decomposition is in heating the material under vacuum conditions to decompose the oxide into O and other constituent elements. In the steady-state process, the main decomposition process takes place in the gas phase. In practice, it is difficult to determine whether the oxide in the gas phase is decomposed or not. However, the thermodynamic behavior of oxides of different elements in the gas phase is different. Thus, a thermodynamic calculation can be used to determine whether the decomposition reaction can be carried out.

The target system composition of thermodynamic calculation is set according to the average composition of lunar soil (total of 100 g) in the operation area of Chang'E−3 (robotic lunar exploration mission operated by the China National Space Administration (CNSA)) exploration area [38], and the thermodynamic equilibrium of the mixed oxide system is calculated by Factsage 8.0 [39,40].

The results in Table 2 reveal that the oxides in lunar soil mainly include SiO_2, TiO_2, Al_2O_3, FeO, MgO, and CaO. Other trace substances are not within the calculation range. These oxides will undergo mineralization, phase transformation, and other processes in the heating process, and eventually gasify into the gas phase. At different temperatures and pressures, the thermodynamic behaviors of different oxides

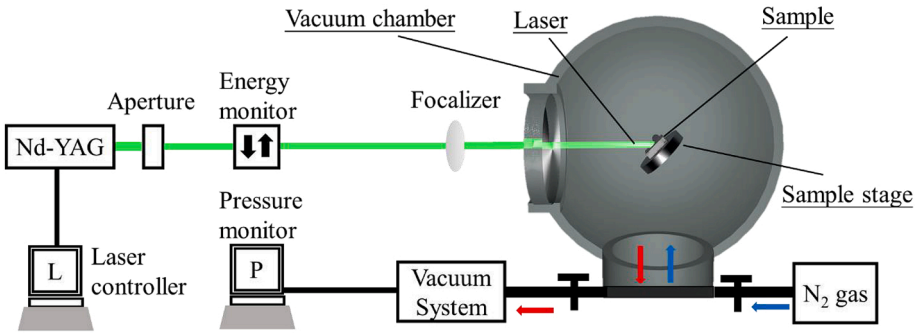

Fig. 3. Schematic diagram of vacuum laser irradiation equipment.

Table 2
Lunar soil composition in the ChangE-3's detection region.

Composition	SiO_2	TiO_2	Al_2O_3	FeO	MgO	CaO	Other
Content (wt%)	41.2	5.0	9.7	22.8	8.1	12.1	1.1

are quite different.

The calculation results are shown in Fig. 4. In the diagrams, the temperature is on the horizontal axis, and the pressure is on the longitudinal axis. The colored area and the marked m (Me_xO_y) indicate the stable pressure stabilizing region of the oxide Me_xO_y in the gas phase. The balance mass at each position in the region can be read out by the

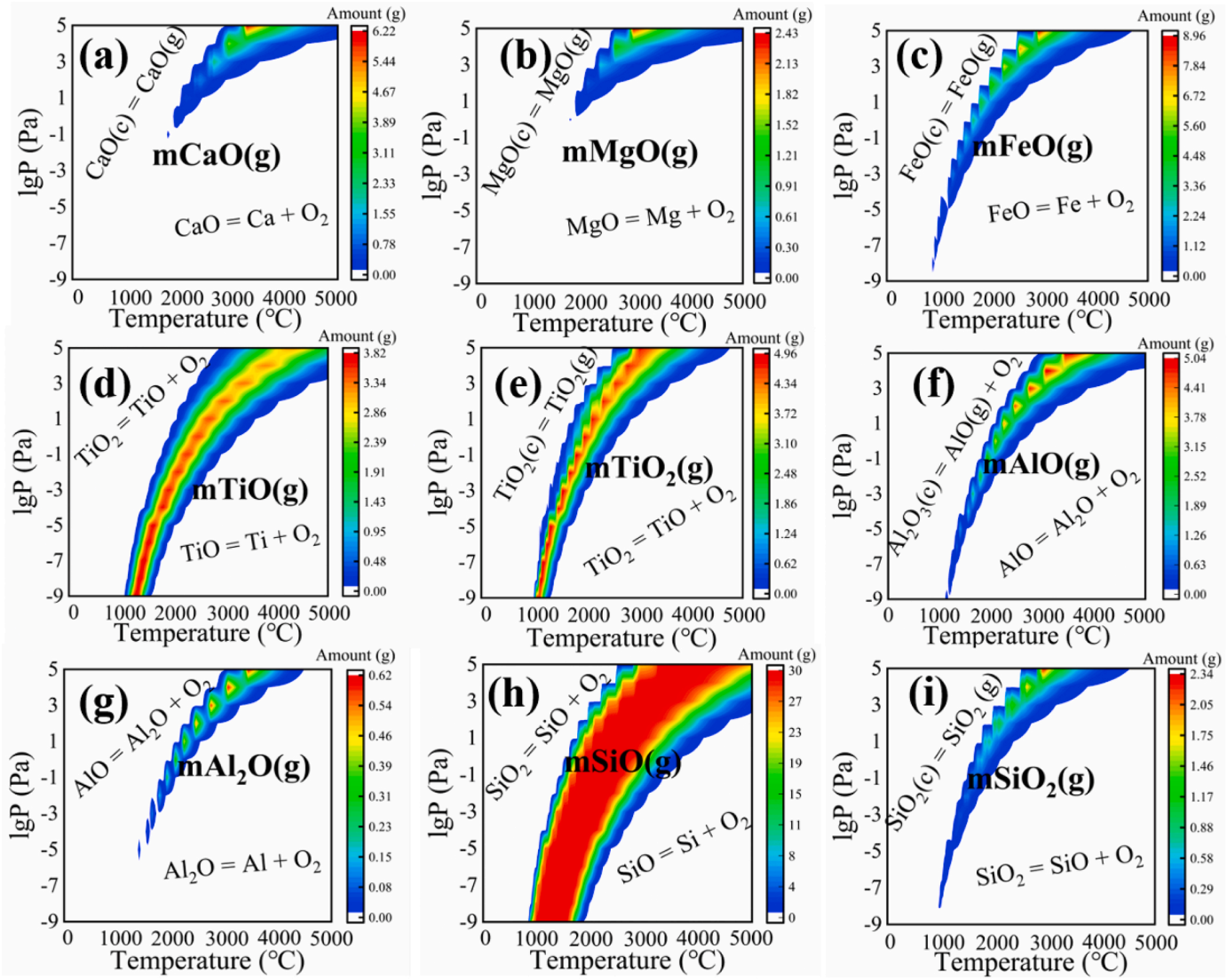

Fig. 4. Thermodynamic stable region and mass of gaseous oxides in simulated lunar soil, (a) CaO stable region and mass; (b) MgO stable region and mass; (c) FeO stable region and mass; (d) TiO stable region and mass; (e) TiO_2 stable region and mass; (f) AlO stable region and mass; (g) Al_2O stable region and mass; (h) SiO stable region and mass; (i) SiO_2 stable region and mass.

corresponding color bar. The reaction equation shown in the upper left corner of the region is the theoretical formation reaction, and the equation shown in the lower right corner is the theoretical decomposition reaction. Due to the existence of various oxide forms in some elements, it is assumed that they are decomposed step by step in the reaction formula shown. With the increase of vacuum degree, the decomposition temperature of all oxides decreases, and the stable temperature range becomes narrower.

As shown in Fig. 4 (a, b), the stability of CaO and MgO in the gas phase decreases with the decrease of the pressure, and the stable range becomes narrower. At the same time, when the pressure is less than a certain value, the gaseous oxides cannot exist stably. Thus, it can be concluded that these two oxides are most easily decomposed [41].

As shown in Fig. 4 (c, f, g, i), FeO, AlO, Al_2O, and SiO_2, respectively, all have similar thermodynamic behavior, and a stable temperature range in a large vacuum range, but their peak content decreases with the decrease of the pressure, thus there is no high oxide content under lower pressure, and it is easy to decompose. This finding indicates that the decomposition products can be extracted by rapid cooling after complete decomposition under low pressure [42].

As shown in Fig. 4 (d, e), for TiO, TiO_2 and other Magnéli phases of Ti oxide, the results show that there is a certain width of the stable temperature range in the calculated pressure range. In addition, the peak content of equilibrium mass increases with the decrease of pressure, which indicates that heating at low pressure will reduce the decomposition temperature, but requires a higher vacuum degree since, even under low pressure, there are a large number of oxides in the gas phase that hinder its decomposition [43].

As shown in Fig. 4 (h), SiO is the most stable of all the calculated oxides. It has the widest stable range and the highest peak content in any pressure range. To achieve the decomposition of SiO into Si and O, the conditions needed are higher than those of any other oxides. At the same time, the distribution of Si resource is the most extensive, and its content in the lunar soil is second only to O. Therefore, the decomposition of SiO is the most difficult and important step of the thermal decomposition process. The thermal decomposition of lunar soil depends on whether Si can be extracted by vacuum thermal decomposition [44].

3.2. Kinetics and transport phenomenon

The COMSOL Multiphysics 5.3 software (COMSOL Inc., Burlington, MA, USA) is used to simulate the heating process of silica heated by nanosecond laser. Since the actual sample is a natural silicon ore, there are many internal grain boundaries, resulting in the great differences in optical properties. As a result, the Lambert Beer's absorption law is not applicable in dealing with this problem due to the difference in optical properties of the raw materials. However, the difference does not affect the thermal conductivity, heat capacity and other basic properties. Therefore, the solid heat transfer method is used to estimate the temperature rise of raw materials irradiated by a single nanosecond laser.

As shown in Fig. 5, under the condition of single laser power of 75 mJ, laser output time of 10 ns and photothermal energy conversion efficiency of 0.1, the silicon oxide can be heated to a high temperature of nearly 4700 °C with only one pulse. According to the results of thermodynamic calculation, the silica should be decomposed into Si and O at low pressure and high power, and completely gasified.

As shown in Fig. 6, the transfer phenomena in the process of pulsed laser irradiation mainly include the following processes:

(a) Plasma emission period: during this period, the main reaction is the process of absorption of the laser irradiation energy by the sample surface, heating, decomposition, and plasma. The laser energy incident on the substrate surface of the sample is attenuated by reflection and refraction. The remaining energy is absorbed by the sample matrix as the reaction energy, which is very short as the output time of the laser is 10 ns. [45–47].

(b) Plasma shielding period: With the excitation of plasma, with higher temperature a layer of vapor or plasma cloud is formed on the surface of silica. The incident laser is absorbed by the plasma cloud before being irradiated on the surface of silica. This part of the material reabsorbs part of the laser energy, contains higher energy density, and decomposes more thoroughly. As the output time of the laser pulse is limited, the duration time of this part is shorter. In the first and second stages, the high-temperature decomposed material is ejected into the gas phase, and then cooled down and homogeneously nucleated, while the completely decomposed oxygen enters the vacuum [48,49].

(c) Plasma radiation period: at this time, the pulsed laser has ended, and the high-temperature decomposition of the plasma cloud has not dispersed. Also, the heat source is the plasma cloud, which radiates heat to the surface of the substrate. At the same time, part of the decomposed high-temperature materials is cooled down and mass transferred to the matrix. This time scale is likely to result in phase transition, part of the heat to overcome the phase transition can make the matrix liquefy, and the emergence of the plasma cloud reduces the influence of the vacuum environment and makes liquefaction possible. At this time, some condensation nucleation gas will enter the thin liquid layer.

(d) Vaporization condensation period: the decomposed high-temperature substance cloud dissipates. Due to the high

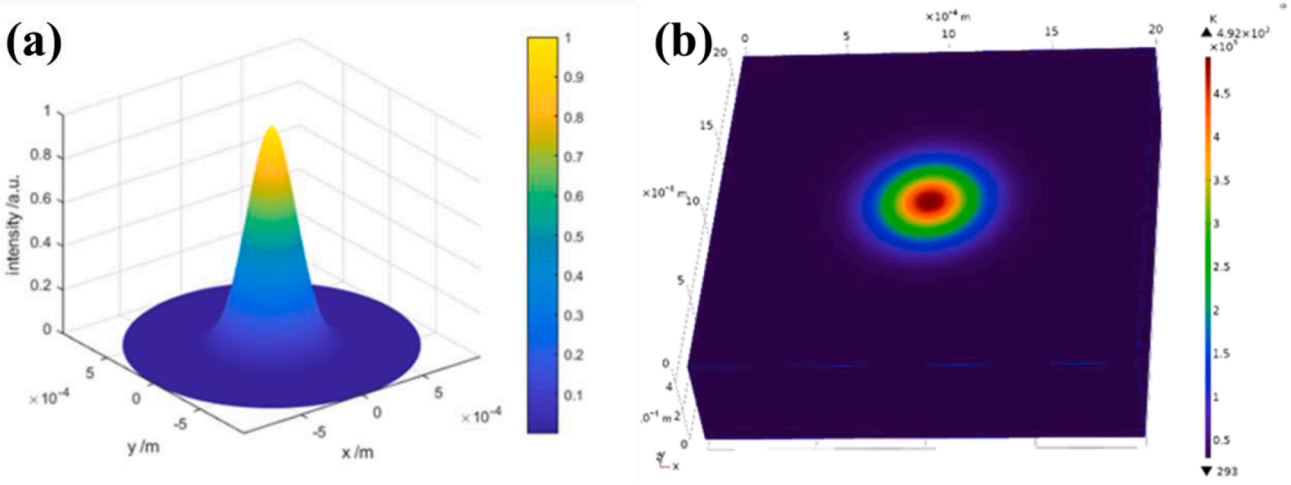

Fig. 5. Energy output of laser source and temperature spatial distribution of silica heated by laser.

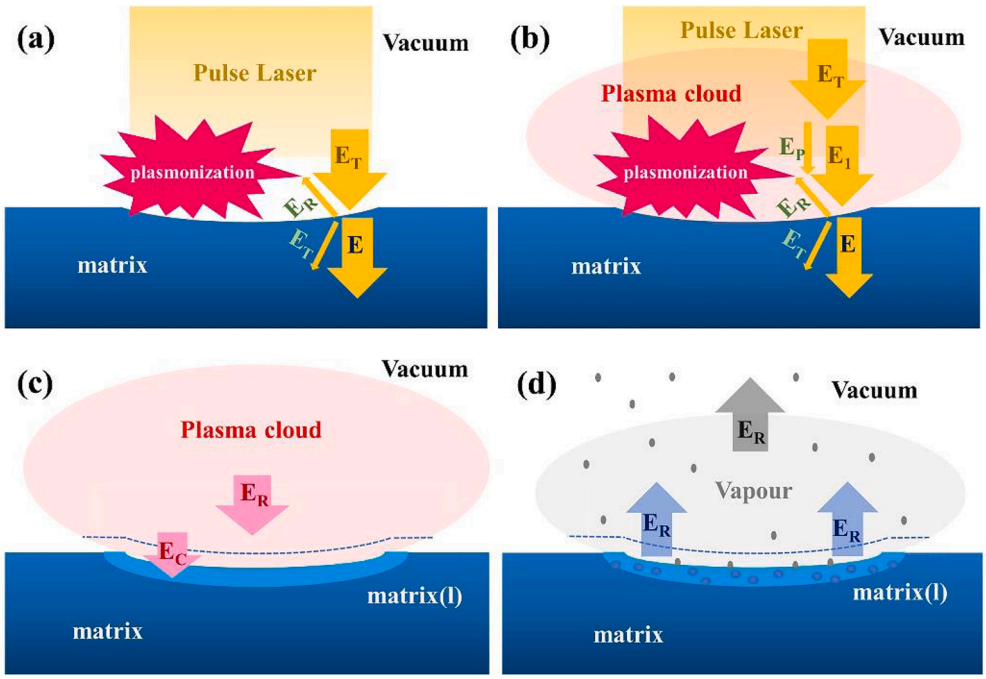

Fig. 6. Transfer phenomena in the process of matrix pulsed laser irradiation. (a) Plasma emission period. (b) Plasma shielding period. (c) Plasma radiation period. (c) Vaporization condensation period.

vacuum environment in the cavity, the surface of the thin liquid layer vaporizes rapidly, so a large amount of heat is dissipated in a short time, and the temperature drops sharply. The liquid phase, which is not gasified, is solidified. Since the quenching condition can be easily achieved with a faster cooling rate, the liquid solidification products obtained are amorphous.

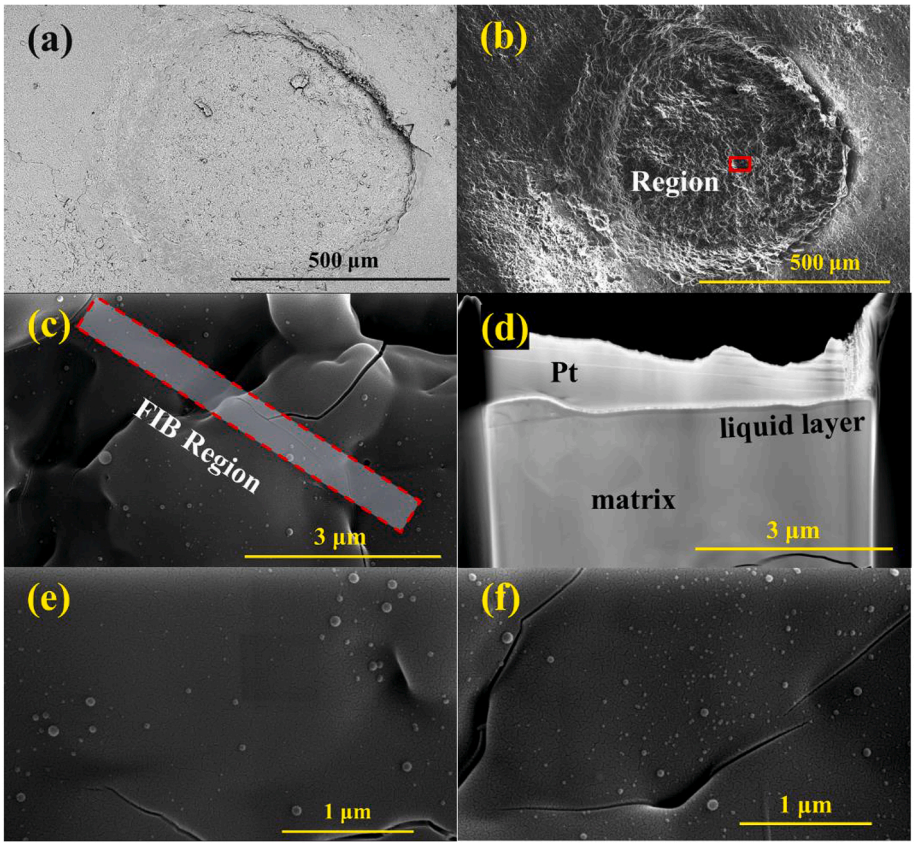

Fig. 7. SEM image of the sample matrix after laser irradiation: (a) T1 mode of whole region; (b) ETD mode of whole region; (c) FIB region of the sample; (d) FIB-slice of the sample; (e, f) Detail view of the surface micromorphology of the sample in ETD mode.

3.3. Vacuum laser decomposition of silicon oxide

As silicon is the element required for resource utilization, and SiO is the most difficult compound to decompose in vacuum, SiO_2 is selected as the sample for the nanosecond laser experiment under vacuum. The SEM images of the surface morphology of quartz after laser irradiation under vacuum examined, shown in T1 mode in Fig. 7 (a), reveals that there is no contrast difference between the irradiated area and the nonirradiated area, and no large-scale chemical composition change in the whole substrate, indicating that a large number of decomposition products are not collected in the substrate. The SEM image of the whole region, shown in ETD mode in Fig. 7 (b), reveals that the diameter of the spot irradiated by pulsed laser is about 650 μm. Also, due to the angle between the incident laser beam and the substrate, the gasification area is an inclined cylinder. It can be observed that the bottom has the typical morphology of surface shrinkage and cracking after liquefaction solidification. This indicates that there is a thin liquid region in the process of transport. In the FIB region and slice (Fig. 7 (c, d) the nano thin liquid layer on the surface is clearly visible and a clear boundary with the matrix is observed. Therefore, the accuracy of the description of the mass transfer process principle can be verified. In addition, a large number of particles, which were nearly spherical with a diameter of 10–150 nm, were found on its surface. According to the dynamic analysis, it can be hypothesized that these particles may be the condensate left after the last laser irradiation.

In the decomposition process, most of the decomposition process is dispersed due to the vacuum condition. As O plasma can combine with oxygen to form O_2, it will disperse at the moment of cooling down. According to thermodynamic calculation, with the decrease of the temperature, the remaining part of silicon and oxygen combine to form SiO, and the excess Si becomes the form of a simple substance, nucleates in the gas phase, and deposits on the copper collecting net. This part of the decomposed sample can be easily collected. For impurities in quartz, independent impurity phases were not found during the experiment, and the degree of ionization of metal ions in the plasma depends on their thermodynamic stability. While H is the least thermally stable of all impurities. During the exposure time of the pulsed laser, substances in the plasma glow have a higher degree of dissociation, while H, which has lower thermodynamic stability, will dissociate first. Relevant studies have shown that at around 1000 °C the solar wind-injected H dissociates [50], while the decomposition reaction of silica occurs in a much higher temperature band.

In addition, due to the reaction force of the plume, the partially decomposed material will return to the thin liquid layer of the matrix. Due to the high temperature, once the surface SiO_2 comes into contact with Si, it will release SiO gas violently. In the process of heat exchange, oxygen is exchanged at the same time, which indicates that there is no stable interface between Si and SiO_2 [51]. Therefore, the decomposition element Si deposited in the basement will not be stable, and SiO_x particles will be reoxidized by oxygen in the thin liquid layer and gas-phase during cooling deposition.

Some regions are not directly attached by plasma, but the surface temperature is increased by radiation heat transfer so that SiO_2 is decomposed into SiO and O_2. A part of the oxygen is generated by this mechanism, which does not produce silicon, and is caused by the waste heat generated by the silicon production reaction when the raw material is reheated.

As shown in Fig. 8, the decomposed products enter the vacuum environment and are collected by the receiving device. The TEM images shown in Fig. 8 (a, b) reveal that the morphology of the decomposed

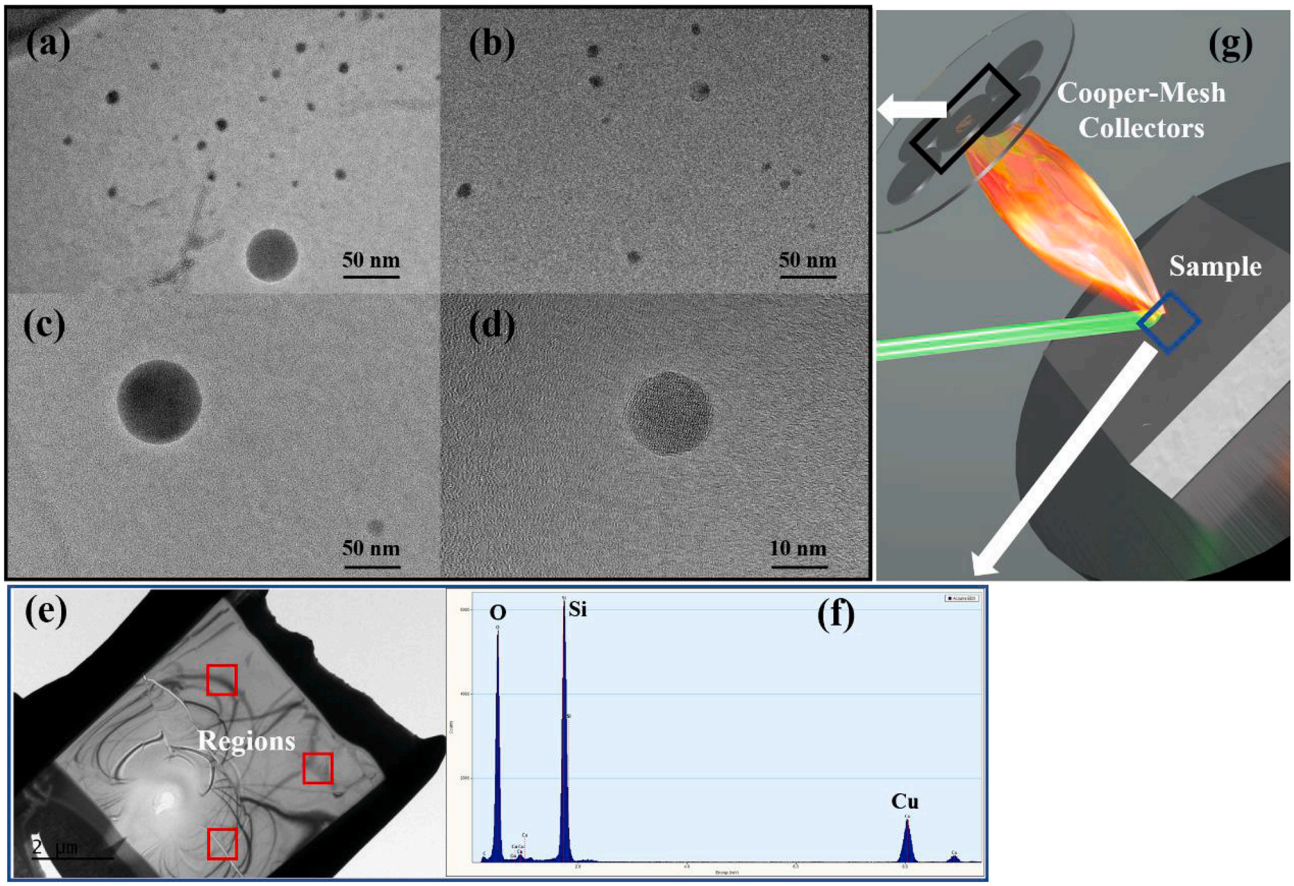

Fig. 8. TEM images of condensation products after laser irradiation. (a–d) Vapor deposition products in cooper-mesh. (e) FIB slice of sample. (f) EDS spectrum of standard SiO_2 matrix. (g) Schematic diagram of sampling area.

product is standard spherical or nearly spherical, its properties are relatively uniform, and its radius is within 100 nm. The number of particles with a larger radius is less than that with a smaller radius. The results show that the decomposed products nucleate uniformly into spheres in the gas phase. As the decomposed gas products are not completely homogeneous jets in the process of laser irradiation, the conditions of condensation are different and the particle sizes are different. These differences mainly include condensation rate, oxygen partial pressure, and temperature. The HRTEM images shown in Fig. 8 (c, d) reveal that the product is amorphous and independent of the radius of the particle. Therefore, it is impossible to determine the phase using lattice calibration for the quantitative analysis. The initial raw material is quartz with a complete crystal structure, which indicates that the collection has undergone a complete decomposition process and nucleated again. For post-decomposition products valence analysis means XPS, EELS are not applicable in this experiment due to the resolution and electron damage properties. Therefore, EDS coupled with TEM was selected to determine its composition.

All particles in the observation area were analyzed quantitatively using the EDS energy spectrum. The data of the EDS energy spectrum can be obtained, and the oxygen silicon atomic ratio O/Si (at%) of the products can be calculated. To correct the quantitative analysis data of the energy spectrum, the FIB slices of the quartz standard sample were prepared using a double beam SEM. As shown in Fig. 8 (e, f), the energy spectrum sampling area of the standard sample was selected inside the sample, and three regions were selected at different positions to take the average value for correction. At the same time, the intensity of the spectral line also revealed that there is no other cation impurity except the background element introduced by the copper mesh. The standard elemental ratio of silica was obtained by energy spectrum analysis of the slices, and then the results of the products were corrected to ensure the accuracy of the results.

The results after correction are shown in Fig. 9. The horizontal axis is the diameter of the particles, and the vertical axis is the atomic ratio after correction. Each point represents the O and Si ratio of particles with different diameters. The error bar on the horizontal axis represents the difference between the long axis and the short axis of the particle and the average particle size. It is a measure of the sphericity of the particle. The vertical axis is the error value of the EDS data output, which is a measure of the content accuracy.

Although the rapid chemical reaction process deviates from the standard state, the tendency of the chemical reaction to proceed can still be determined by the Gibbs free energy criterion. When steam and tiny droplets coexist in ultra-high vacuum, the Gibbs free energy of both can be expressed in different equations:

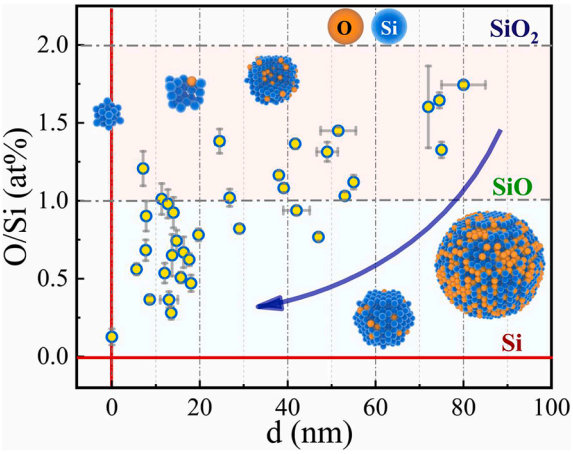

Fig. 9. Scatter diagram of the chemical composition of the condensation products with different diameters.

$$G(p_{vacuum}) = G^{\Theta} + RT_{vapor-liquid} \ln \frac{p_{vacuum}}{p^{\Theta}} \quad (1)$$

Equation (1) is the expression of the Gibbs free energy of gaseous substances under vacuum conditions, which is formed by the Gibbs free energy isotherm equation and the ideal gas state equation. where p_{vacuum} is the air pressure in a high vacuum environment, $G(p_{vacuum})$ is the Gibbs free energy of the vacuum vapor substance, and G^{Θ} is the Gibbs free energy in the standard state. Since the gas pressure under vacuum is much lower than the standard gas pressure, the volume-increasing reaction tends to increase (such as the decomposition of SiO_2).

$$G(p_{droplets}) = G^{\Theta} + RT_{vapor-liquid} \ln \frac{p^{\Theta} + 2\sigma/r}{p^{\Theta}} \quad (2)$$

Equation (2) is the expression of the Gibbs free energy of agglomerated tiny droplets, which is formed by the Gibbs free energy isotherm equation and the Kelvin equation simultaneously. where $p_{droplets}$ is the vapor pressure of the tiny droplets, σ is the surface tension of the liquid, and r is the radius of the droplet. From this relationship, we can see that the smaller the radius of the particle, the greater the additional pressure and the greater the saturated vapor pressure. According to the difference between equation (1) and equation (2) according to the relationship between the gas product and the residual reactant, it can be known that the higher the vacuum degree and the smaller the radius of the particle reaction in thermodynamics, the stronger the trend is. The same conclusion can also be obtained by simple analysis of kinetics.

The results in Fig. 9 show that the number of particles increases with the decrease of particle diameter. The atomic ratio of O and Si is lower than that of SiO_2. The results also reveal that the smaller the particle size, the more complete the decomposition. At the same time, the ratio of O to Si of many particles is less than 1:1, which indicates that laser heating can cross the stable region of SiO and achieve complete decomposition. Also, with the decrease of the particle radius, the ratio of O to Si decreases. The minimum value for the surface film layer (diameter close to 0) is 0.12. This may be due to the complete decomposition in the decomposed gas phase and the difference of oxygen partial pressure in each position during the homogeneous nucleation process, so that Si will preferentially nucleate and condense, while O will combine with oxygen in vacuum due to the reduction of Si in the gas phase and high vacuum condition. The oxygen which does not diffuse in time in the atmosphere will oxidize the Si particles to different degrees. As the cooling rate of the larger particles is slower, the oxidation rate of the larger particles is much faster than that of the small particles. The oxidation of Si releases more heat, which slows down the cooling rate of the particles and increases the oxidation rate. The O/Si ratio of the condensation product is always lower than that of SiO_2 because some O-junction synthesized oxygen is still dispersed. Since part of the oxygen in the product comes from the gas oxidation during sampling and loading, which cannot be avoided under the current conditions, the Si content of the product should be higher than that of the data.

4. Conclusion

The following conclusions can be drawn from this study:

The vacuum thermal stability of the main oxides of lunar soil has been proved by thermodynamic calculation under ultra-high vacuum. And according to the thermodynamic behavior of oxide decomposition, it is divided into: easily decomposable oxides (MgO and CaO), decomposable oxides (FeO, AlO, Al_2O, and SiO_2), refractory decompose oxides (TiO and TiO_2) and extremely difficult decompose oxide (SiO). This provides a theoretical prototype for the study of vacuum thermal decomposition of oxides on the lunar surface.

In this study, a pulsed laser was used as a heat source to explore the decomposition behavior of silicon oxide under ultra-high vacuum conditions, combined with temperature field calculation, thermodynamic analysis, kinetic process prediction, product micro-area analysis and

chemical composition calibration. shows that Under the conditions of 75 mJ pulse energy, 532 nm pulse laser wavelength, 10^{-4} Pa initial pressure and 0.2 Hz frequency irradiation for 50 cycles. The condensation product of decomposition of silicon oxide consists of amorphous spherical particles with a size of below 100 nm. The silicon-oxygen ratio of the product ranges from 1.74 to 0.12 revealed that decomposition reactions have occurred. The inverse relationship between the degree of decomposition and the particle radius indicates a synergistic relationship between the vacuum environment and surface tension during vacuum thermal decomposition. This study illustrates the broad application prospect of vacuum thermal decomposition method for lunar surface resource extraction.

CRediT authorship contribution statement

Chen Li: Investigation, Methodology, Writing – original draft. **Kuixain Wei:** Supervision, Funding acquisition. **Yang Li:** Writing – review & editing, Conceptualization. **Wenhui Ma:** Project administration. **Sizhe Zhao:** Resources. **Han Yu:** Visualization. **Zhuang Guo:** Formal analysis. **Jianzhong Liu:** Validation.

Declaration of competing interest

The authors declare that they have no known competing financial interests or personal relationships that could have appeared to influence the work reported in this paper.

Acknowledgements

The financial support of this research work was provided by the Yunnan Outstanding Youth Science Foundation (No. 202101AV070007), the Reserve Talents of Young and Middle-aged Academic and Technical Leaders in Yunnan Province (No. 2018HB009). Strategic Priority Research Program of the Chinese Academy of Sciences grant XDB 41000000.

Appendix A. Supplementary data

Supplementary data to this article can be found online at https://doi.org/10.1016/j.vacuum.2022.111162.

References

[1] G.H. Heiken, D.T. Vaniman, B.M. French, 1991.
[2] J. Rasera, J. Cilliers, J.-A. Lamamy, K. Hadler, Planet. Space Sci. (2020), 104879.
[3] A.H. Cutler, P. Krag, in: Lunar Bases and Space Activities of the 21st Century, 1985, p. 559.
[4] R.P. Mueller, I. Townsend, I. Ivan, J.G. Mantovani, in: Earth and Space 2010: Engineering, Science, Construction, and Operations in Challenging Environments, 2010, pp. 1353–1363.
[5] R. Gustafson, B. White, M. Fidler, A. Muscatello, in: 48th AIAA Aerospace Sciences Meeting Including the New Horizons Forum and Aerospace Exposition, 2010, p. 1163.
[6] H.N. Friedlander, in: Lunar Bases and Space Activities of the 21st Century, 1985, p. 611.
[7] G.B. Sanders, W.E. Larson, in: American Society of Civil Engineers, 2012.
[8] H. Sargeant, F. Abernethy, M. Anand, S. Barber, P. Landsberg, S. Sheridan, I. Wright, A. Morse, Planet. Space Sci. 180 (2020), 104759.
[9] M. Hasegawa, in: Treatise on Process Metallurgy, Elsevier, 2014, pp. 507–516.
[10] D. Sadoway, A. Ignatiev, P. Curreri, E. Carol, LPI Contrib. 2152 (2019) 5012.
[11] L. Sibille, S. Schreiner, J. Dominguez, LPI Contrib. 2152 (2019) 5100.
[12] L. Sibille, D. Sadoway, A. Sirk, P. Tripathy, O. Melendez, E. Standish, J. Dominguez, D. Stefanescu, P. Curreri, S. Poizeau, in: 47th AIAA Aerospace Sciences Meeting Including the New Horizons Forum and Aerospace Exposition, 2009, p. 659.
[13] S. Schreiner, L. Sibille, J. Dominguez, A. Sirk, J. Hoffman, G. Sanders, in: 8th Symposium on Space Resource Utilization, 2015, p. 1180.
[14] T. Matsumoto, D. Harries, F. Langenhorst, A. Miyake, T. Noguchi, Nat. Commun. 11 (2020) 1–8.
[15] B. Hapke, J. Geophys. Res.: Planets 106 (2001) 10039–10073.
[16] M. Anand, L.A. Taylor, M.A. Nazarov, J. Shu, H.-K. Mao, R.J. Hemley, Proc. Natl. Acad. Sci. 101 (2004) 6847–6851.
[17] S. Sasaki, K. Nakamura, Y. Hamabe, E. Kurahashi, T. Hiroi, Nature 410 (2001) 555–557.
[18] R.A. Wiesli, B.L. Beard, L.A. Taylor, C.M. Johnson, Earth Planet Sci. Lett. 216 (2003) 457–465.
[19] H. Tang, S. Wang, X. Li, Planet. Space Sci. 60 (2012) 322–327.
[20] P. Szabo, H. Biber, N. Jäggi, M. Wappl, R. Stadlmayr, D. Primetzhofer, A. Nenning, A. Mutzke, J. Fleig, K. Mezger, J. Geophys. Res.: Planets 125 (2020) e2020JE006583.
[21] L.V. Moroz, L.V. Starukhina, S.S. Rout, S. Sasaki, J. Helbert, D. Baither, A. Bischoff, H. Hiesinger, Icarus 235 (2014) 187–206.
[22] T. Kohout, J. Čuda, J. Filip, D. Britt, T. Bradley, J. Tuček, R. Skála, G. Kletetschka, J. Kašlík, O J I, Malina 237 (2014) 75–83.
[23] A. Fazio, D. Harries, G. Matthäus, H. Mutschke, S. Nolte, F. Langenhorst, Icarus 299 (2018) 240–252.
[24] D. Wingo, LPI Contrib. 2152 (2019) 5098.
[25] E.H. Cardiff, B.R. Pomeroy, I.S. Banks, A. Benz, in: AIP Conference Proceedings, American Institute of Physics, 2007, pp. 846–853.
[26] M. Anand, I.A. Crawford, M. Balat-Pichelin, S. Abanades, W. van Westrenen, G. Péraudeau, R. Jaumann, W. Seboldt, Planet. Space Sci. 74 (2012) 42–48.
[27] T. Yabe, K. Ikuta, C. Baasandash, R. Katano, S. Uchida, M. Tsuji, Y. Mori, J. Maehara, M.S. Mahmoud, T. Toya, in: AIP Conference Proceedings, American Institute of Physics, 2006, pp. 447–456.
[28] T. Yabe, K. Yoshida, S. Uchida, in: International Congress on Applications of Lasers & Electro-Optics, Laser Institute of America, 2007, p. M1103.
[29] T. Yabe, M. Mohamed, S. Uchida, C. Baasandash, Y. Sato, M. Tsuji, Y. Mori, J. Appl. Phys. 101 (2007), 123106.
[30] T. Yabe, T. Ohkubo, S. Uchida, K. Yoshida, M. Nakatsuka, T. Funatsu, A. Mabuti, A. Oyama, K. Nakagawa, T. Oishi, Appl. Phys. Lett. 90 (2007), 261120.
[31] Y. Sato, T. Yabe, Y. Sakurai, M. Mohamed, S. Uchida, C. Baasandash, T. Ohkubo, Y. Mori, H. Sato, in: AIP Conference Proceedings, American Institute of Physics, 2008, pp. 546–552.
[32] M. Mohamed, T. Yabe, C. Baasandash, Y. Sato, Y. Mori, L. Shi-Hua, H. Sato, S. Uchida, J. Appl. Phys. 104 (2008), 113110.
[33] S. Tanaka, S. Yamada, K. Komurasaki, H. Koizumi, J. Thermophys. Heat Tran. 34 (2020) 733–740.
[34] S. Tanaka, S. Yamada, K. Komurasaki, H. Koizumi, in: AIAA Propulsion and Energy 2019 Forum, 2019, p. 4161.
[35] S. Nakashima, H. Matayoshi, T. Yuko, K. Michibayashi, T. Masuda, N. Kuroki, H. Yamagishi, Y. Ito, A. Nakamura, Tectonophysics 245 (1995) 263–276.
[36] Y. Liu, Y. Guan, Y. Zhang, G.R. Rossman, J.M. Eiler, L.A. Taylor, Nat. Geosci. 5 (2012) 779–782.
[37] C.M. Pieters, S.K. Noble, J. Geophys. Res.: Planets 121 (2016) 1865–1884.
[38] Z. Ling, B.L. Jolliff, A. Wang, C. Li, J. Liu, J. Zhang, B. Li, L. Sun, J. Chen, L. Xiao, Nat. Commun. 6 (2015) 1–9.
[39] C.W. Bale, P. Chartrand, S. Degterov, G. Eriksson, K. Hack, R.B. Mahfoud, J. Melançon, A. Pelton, S. Petersen, Calphad 26 (2002) 189–228.
[40] C.W. Bale, E. Bélisle, P. Chartrand, S. Decterov, G. Eriksson, A. Gheribi, K. Hack, I.-H. Jung, Y.-B. Kang, J. Melançon, Calphad 55 (2016) 1–19.
[41] R. Huang, P. Liu, X. Qian, J. Zhang, Vacuum 134 (2016) 20–24.
[42] M. Halmann, A. Steinfeld, M. Epstein, I. Vishnevetsky, Miner. Process. Extr. Metall. Rev. 35 (2014) 126–135.
[43] A.A. Valeeva, S.Z. Nazarova, H. Schröttner, E.Y. Gerasimov, A.A. Rempel, RSC Adv. 10 (2020) 25717–25720.
[44] P.G. Loutzenhiser, O. Tuerk, A. Steinfeld, JOM 62 (2010) 49–54.
[45] A.A. Martin, N.P. Calta, S.A. Khairallah, J. Wang, P.J. Depond, A.Y. Fong, V. Thampy, G.M. Guss, A.M. Kiss, K.H. Stone, C.J. Tassone, J. Nelson Weker, M. F. Toney, T. van Buuren, M.J. Matthews, Nat. Commun. 10 (2019) 1987.
[46] W. Zhao, X. Shen, H. Liu, L. Wang, H. Jiang, Opt Laser. Eng. 124 (2020).
[47] Y. Zhang, J. Zhang, Addit. Manuf. 16 (2017) 49–57.
[48] L. Xia, J. Chen, K. Liao, L. Huang, Q. Li, X. Luo, Mater. Sci. Semicond. Process. 105 (2020).
[49] F. Wirth, K. Wegener, Addit. Manuf. 24 (2018) 249–256.
[50] X. Zeng, H. Tang, X. Li, X. Zeng, W. Yu, J. Liu, Y. Zou, Earth Planet Sci. Lett. 560 (2021), 116806.
[51] H. Fujii, M. Yamamoto, S. Hara, K. Nogi, J. Mater. Sci. 34 (1999) 3165–3168.